Shape of growth cells in directional solidification

A. Pocheau* and M. Georgelin†
IRPHE, CNRS & Universités Aix-Marseille I & II, 49 rue Joliot-Curie, B.P. 146, Technopôle de Château-Gombert, F-13384 Marseille, Cedex 13, France
(Received 14 July 2005; published 19 January 2006)

The purpose of this study is to characterize experimentally the *whole* shape of the growth cells displayed in directional solidification and its evolution with respect to control parameters. A library of cells is first built up from observation of directional solidification of a succinonitrile alloy in a large range of pulling velocity, cell spacing, and thermal gradient. Cell boundaries are then extracted from these images and fitted by trial functions on their whole profile, from cell tip to cell grooves. A coherent evolution of the fit parameters with the control parameters is evidenced. It enables us to characterize the *whole* cell shape by a *single* function involving only *two* parameters which vary *smoothly* in the control parameter space. This, in particular, evidences a continuous evolution of the cell geometry at the cell to dendrite transition which denies the existence of a change of branch of solutions at the occurrence of sidebranching. More generally, this global determination of cell shape complemented with a previous determination of the position of cells in the thermal field (the cell tip undercooling) provides a complete characterization of growth solutions and of their evolutions in this system. It thus brings about a relevant framework for testing and improving theoretical and numerical understanding of cell shapes and cell stability in directional solidification.

DOI: 10.1103/PhysRevE.73.011604 PACS number(s): 81.10.Aj, 81.30.Fb, 05.65.+b, 47.54.−r

I. INTRODUCTION

Out-of-equilibrium systems involving different thermodynamic phases usually seek to recover equilibrium by displacing phase interfaces. Examples of this can be found in systems dominated by capillary forces (e.g., dewetting transition), energy release (e.g., premixed combustion), or liquid-solid transformation (e.g., crystal growth). In these issues, growth interfaces stand as free boundaries, not prescribed in advance, which fix boundary conditions to the fields which govern the different phases in contact. In particular, their geometry takes part in the determination of the exchange flux between the different phases and thus in the way these systems adapt themselves to the out-of-equilibrium conditions. Accordingly, solving for the shape of growth interfaces is mainly solving for the behavior of the corresponding systems in out-of-equilibrium regimes.

The purpose of this work is to experimentally determine the shapes of the steadily growing cells displayed in directional solidification from the cellular regime to the near dendritic regime. By "shape," we do not understand here the form of truncated parts of cells but, instead, their *whole* profile from their tip to their grooves. Our goal will then be to determine their geometry by a *single*, simple but relevant algebraic *function*, parametrized by the control parameters of the system through deterministic, analytic, *combinations*.

Here, the term "simple" means that the search for the shape function will not be ascribed to detailed mathematical considerations about possible cell profiles in definite regions but, instead, will be guided by a heuristic analysis of the system. In particular, the family of trial functions will involve parameters all relying on physically meaningful features and whose number will be kept to the minimum. Interestingly, the latter feature will provide these parameters with the opportunity of referring not only to optimal analytical values but also to relevant physical considerations. In the same spirit, requiring that the fit parameters express as "analytic combinations" of the control parameters means that we do not simply seek to recover the shape of each cell *separately* with *ad hoc* fit parameters but that we aim, instead, at determining a *global representation* of the geometry displayed by the growth system as its control parameters are varied. To this goal, the generating function which gives a global parametrization of the *whole family* of cellular interface shapes will have to display *coherent* variations of its fit parameters with the control parameters of the system. This, of course, will be all the more easy to achieve that the number of its fit parameters will be small.

The advantages of a global determination of steady interface shapes are many. Beyond the fact that this has never been achieved to-date, the need for such a determination is stressed by the formal difficulties encountered in deriving the shapes of steady cells analytically and in comparing them to the observed ones on a rational basis. In particular, calling Λ the cell spacing, V the pulling velocity, D the diffusivity of the dominant impurity, and $Pe=\Lambda V/D$ the resulting Péclet number, analytical determinations of cell shapes in term of Saffman-Taylor fingers (Ivantsov paraboloids [1]) have been achieved in the low Péclet number limit $Pe \ll 1$ where cells are diffusively coupled [2] (respectively in the large Péclet number limit $Pe \gg 1$ where cells are isolated [3]). However, in the intermediate Péclet number regime, $Pe=O(1)$, that is relevant to experiments, direct analysis of forms [4] as well as analysis of their resulting position in the thermal-gradient [5] have rejected these two families of forms as suitable candidates for modelling the cellular shapes. Matched

*Electronic address: alain.pocheau@irphe.univ-mrs.fr
†Electronic address: marc.georgelin@irphe.univ-mrs.fr

asymptotic expansions have then been performed to conciliate analyses specific to definite cell regions [6,7]. However, they have addressed either the large velocity regime which pertains to strong sidebranching [7] or the small Péclet number regime $Pe \ll 1$ [6] which is hardly reached by experiments and, in both cases, provided no explicit determination of cell shapes. Despite the important progress they bring towards a global solution for directional growth, they thus do not offer an easy access to a direct comparison with steady experimental shapes.

In this context, an empirical determination of steady cell shapes is thus likely to improve our understanding of growth shapes by providing a definite *synthetized* expression for the shape *library*. In particular, it should then worth comparing this library to numerical simulations or theoretical determinations in similar growth conditions or directly use it to numerically investigate, on appropriate shapes, the stability of cells or of cell arrays. Also, on the theoretical side, this global determination of the free-boundary solution of the growth system may be expected to stimulate improved analysis of growth equilibrium and of the resulting large scale properties of growth interfaces.

Our analysis of the shape library will provide an accurate and global determination of two fitting parameters with a strong geometrical significance: the radius of curvature ρ at the cell tip and the width L of the solid phase in between the grooves. Here the term "global" means that these parameters are determined, not from *parts* of a *single* cell but, instead, from the *whole* cell shapes observed in the *whole* studied regimes. On the other hand, a detailed comparison between the steady shapes found in the cellular regime and the mean shapes observed in the near dendritic regime will enable us to state whether a change of branch of solution arises at the occurrence of sidebranching. Both results will clarify the cell geometry, its evolution with control parameters and the nature of the cell to dendrite transition.

The article is organized as follows. The experimental context is reported in Sec. II and the methodology applied for pointing out a global shape function is discussed in Sec. III. The determination of this function and of its parameters is reported in Sec. IV. It involves an individual optimization, a collective optimization, a validation and a test for robustness. A synthesis of the evolution of cell shape and cell position with control parameters is reported in Sec. V. Section VI is devoted to a discussion about of these results and Sec. VII to a conclusion about the implications of this study.

II. EXPERIMENT

A. Experimental setup

Following Jackson and Hunt [8], the experimental setup is designed so as to pull a thin sample of mixture within a thermal gradient at a fixed velocity (Fig. 1). Special care has been taken to satisfy the steadiness of the pulling velocity and the spatial uniformity of the sample depth, of the thermal gradient, and of the crystal orientation [9].

The pulling stage is provided by a linear ball-screw monitored by a micro-stepper motor. The relative accuracy of the pulling velocity is $\delta V/V=3\%$ over a screw pitch (5 mm). It

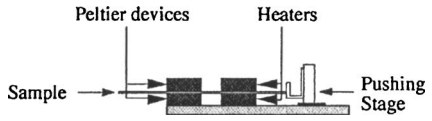

FIG. 1. Sketch of experimental setup.

is controlled in real time by a Michelson interferometer. Both heaters and coolers are made of two metallic blocks, 1 cm thick, 5×5 cm^2 wide that sandwich the sample. Heating is provided by a resistance sheet or a Peltier device, both electronically regulated to better than 10^{-1} K. Thermal blocks are nominally maintained at a temperature of 10 °C and 100 °C. They are separated by a gap g which has been set to 5 mm or 10 mm, thereby yielding a thermal gradient of 78 K cm^{-1} or 140 K cm^{-1} [10].

Samples are made of two glass plates 45 mm $\times$ 100 mm that sandwich 50 μm thick spacer sheets. They are filled with succinonitrile purchased from Sigma Chemical Co., St. Louis whose purity is at least 99.6 mass%. They are glued on their sides so as to achieve airtightness. To avoid end effects, only bulk cells are studied in a central region, 25 mm large, that stands 10 mm away from each boundary. As the typical cell spacing is 100 μm, about 250 cells standing at a distance of 100 cells from the boundaries can thus be studied.

A nuclear magnetic resonnance (NMR) study has revealed an ethylenic bond [5]. This points to ethylene as the dominant impurity of the mixture. In particular, the fact that IR spectroscopy revealed no trace of chemical bonds characteristic of water denies any measurable contamination of our samples by this substance. The solutal diffusivity of the impurity in the liquid phase D has been deduced from accurate measurement and analysis of the temperature of cell tips [5]: $D=1.35\pm0.05\times10^{-5}$ cm^2 s^{-1}. The partition coefficient k of the mixture has been determined from measurements of the melting and solidifying temperatures of planar fronts: $k\approx0.29\pm0.05$. The corresponding value of the ratio D/k has been confirmed by the study of the relaxation time $D/(kV^2)$ of a planar front to an equilibrium position in the thermal field. The liquidus slope m and the mean solute concentration c_∞ have not been measured separately, but their product, mc_∞, which amounts to the difference between the liquidus temperature of the mixture, T_L, and the melting temperature of pure succinonitrile, T_0, has been measured to 2.0 K. It corresponds to a temperature difference $T_L-T_S=mc_\infty(1-k)/k$ of about 5 K between liquidus and solidus in the mixture. This yields critical velocities $V_c=DG/(T_L-T_S)$ for planar destabilization ranging from 2 μm s^{-1} at $G=78$ K cm^{-1} to 4 μm s^{-1} at $G=140$ K cm^{-1}, as confirmed experimentally. Notice finally that, according to the thermodynamical relationships for dilute alloys, the ratio $m/(1-k)$ only depends on the solvent, succinonitrile here. In particular, literature shows that its value ranges from 2.45 K mol %$^{-1}$ [11] to 2.50 K mol %$^{-1}$ [12]. Taking the average value and our determination of k yields $m\approx1.75\pm0.15$ K mol %$^{-1}$ and finally $c_\infty=1.15\pm0.1$ mol %. Given the molar weight $M=80.09$ g of succinonitrile and its concentration 99.6 mass%, the measured impurity concentration c_∞ corresponds to a mean molar mass $M'=27\pm5$ g, in agreement with ethylene (28 g). This corroborates the conclusion of the NMR and IR analyses.

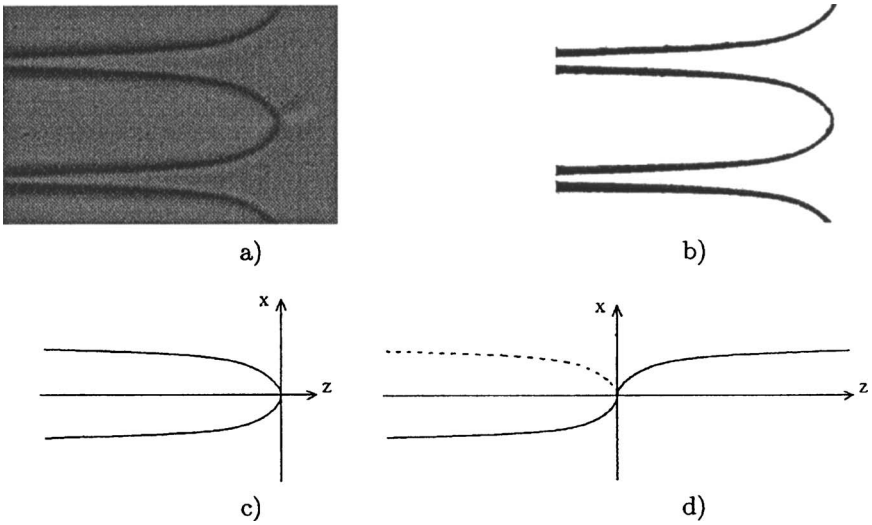

FIG. 2. Image processing on an experimental picture. A snapshot of a cell (a) is smoothed, binarized (b), and skeletonized (c). A symmetry is then applied on half of the curve so as to obtain a single-valued representation (d).

Succinonitrile being a plastic crystal, its growth is favored along its crystalline axes. To ensure measurement reproducibility and concentrate on the sole effect of macroscopic control parameters, the preferred growth directions must then be kept as uniform as possible on the sample. For this, a definite orientation has then been chosen and applied on the whole sample by selecting and enhancing those monocrystal domains whose crystalline axes were parallel to the pulling direction, the thermal gradient, and the cell depth [9]. In order to avoid spurious variations of experimental conditions, all the forms investigated here were obtained in the same sample.

To preserve a large zone free of instrumental disturbance around the front, an exploded optical setup has been used so as to work with large frontal distances. Magnifications from 2 to 40 were available. The images of the growth front have been recorded via a CCD camera on a time-lapse video recorder, and then digitalised at a resolution of 768×512 pixels on 256 gray levels. After binarization, the liquid-solid interface appears as a thick line, about five pixels large [Fig. 2(a)]. It is then skeletonized [Fig. 2(b)] to reduce the front to a single pixel thick line [Fig. 2(c)], which has further to be fitted by a relevant mathematical function. For this, it appears convenient to apply a symmetry on half of the front to obtain a single-valued function [Fig. 2(d)].

B. Cellular regime; dendritic regime

Above the critical value V_c, the planar front destabilizes onto an array of cells whose typical spacing is of order a hundred microns (Fig. 3). Their grooves, initially shallow, grow with the pulling velocity, and become deeper than three cell spacings above about $3/2\ V_c$. In this long-groove regime, too large or too thin cells are unstable by the various modes of instability of one-dimensional cellular patterns [13]. Above a critical value $V_s(\Lambda, G)$ dependent on the cell spacing Λ and on the thermal gradient G, cells develop sidebranches [Figs. 4(a), 5(c), and 6(b)] [9] whose amplitudes rise with the pulling velocity [Figs. 4(c) and 6(c)]. However, they remain shorter than $\Lambda/10$ for $V < 2.5V_s$. This will be taken here as the definition of the moderately dendritic regime: $V_s < V < 2.5V_s$.

The present study has taken place from within the domain of long-groove stable cells $3/2\ V_c < V < V_s$ to the moderately dendritic regime $V_s < V < 2.5V_s$. The scanning ranges of cell spacing and of pulling velocity have been $50 < \Lambda < 170\ \mu\text{m}, 8 < V < 24\ \mu\text{m s}^{-1}$ and two thermal gradients have been investigated: $G = 78$ K cm^{-1} to 140 K cm^{-1}. Scale ranges have thus extended over a factor 3 for both Λ and V and a factor 2 for G. Within them, tip cells got more and more sharp as the pulling velocity or the cell spacing were increased or the thermal gradient decreased. This is apparent in Figs. 3–6 where a set of cell shapes representative of the database are compared for increasing cell spacing, velocity, or thermal gradient.

C. Steadiness and uniformity

To be meaningful, the determination of cell shapes must not depend on uncontrolled or undetermined conditions.

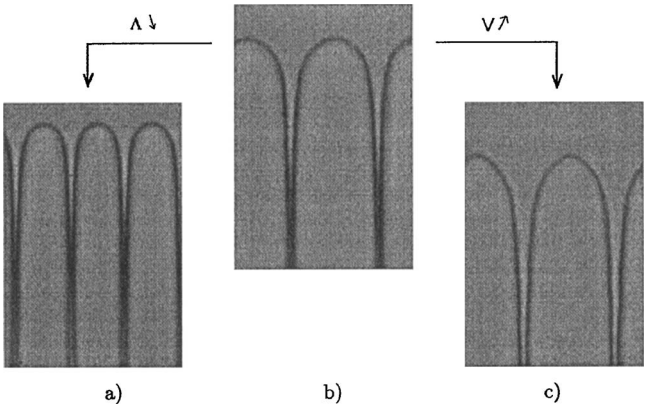

FIG. 3. Cell geometry at $G = 140$ K cm^{-1}. Evolution with cell spacing at fixed velocity and gradient [(a) to (b)], and with velocity at fixed spacing and gradient [(b) to (c)]. Increasing velocity sharpens tip cell. Changing spacing nearly keeps the tip geometry unchanged. (a) $(V, \Lambda, G) = (12, 50, 140)$ (μm s^{-1}, μm, K cm^{-1}); (b) $(V, \Lambda, G) = (12, 90, 140)$ (μm s^{-1}, μm, K cm^{-1}); (c) $(V, \Lambda, G) = (24, 90, 140)$ (μm s^{-1}, μm, K cm^{-1}).

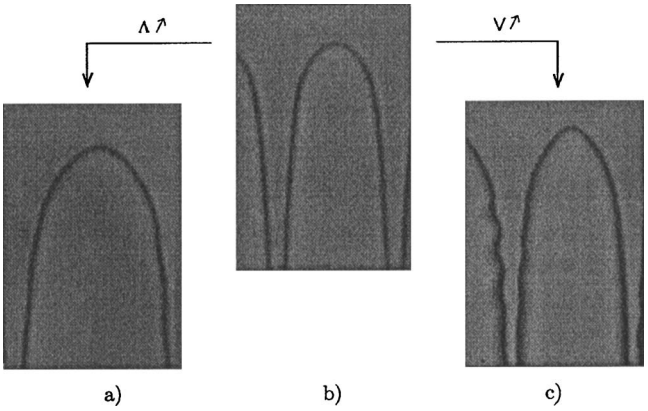

FIG. 4. Cell geometry at $G=78\ \mathrm{K\ cm^{-1}}$. Evolution with cell spacing at fixed velocity and gradient [(a) to (b)], and with velocity at fixed spacing and gradient [(b) to (c)]. Increasing velocity sharpens tip cell. Changing spacing nearly keeps the tip geometry unchanged. (a) $(V,\Lambda,G)=(8,170,78)$ $(\mu\mathrm{m\ s^{-1}},\mu\mathrm{m},\mathrm{K\ cm^{-1}})$; (b) $(V,\Lambda,G)=(8,120,78)$ $(\mu\mathrm{m\ s^{-1}},\mu\mathrm{m},\mathrm{K\ cm^{-1}})$; (c) $(V,\Lambda,G)=(20,120,78)$ $(\mu\mathrm{m\ s^{-1}},\mu\mathrm{m},\mathrm{K\ cm^{-1}})$.

This, in particular, calls for uniform mixture, steady states, and uniform cellular patterns. The two first requirements will ensure that neither the growth history nor the initial conditions take part in the cell geometry; the latter requirement will allow the cell shape to be representative of its own spacing without explicit reference to its environment.

Following microsegregation, the solidified mixture exhibits inhomogeneities of impurity concentration on characteristic scales of the order of the cell sizes Λ (the diffusion length l_D) on the directions normal (parallel) to the thermal gradient. When melted again, these inhomogeneities relax by diffusion in the liquid phase in a time of order $\Lambda^2/D(l_D^2/D)$ [14]. In both cases, the longest of these characteristic times is of the order of 20 *s*. As samples are fully melted during a much larger time, about 1 h, before solidifying, segregation

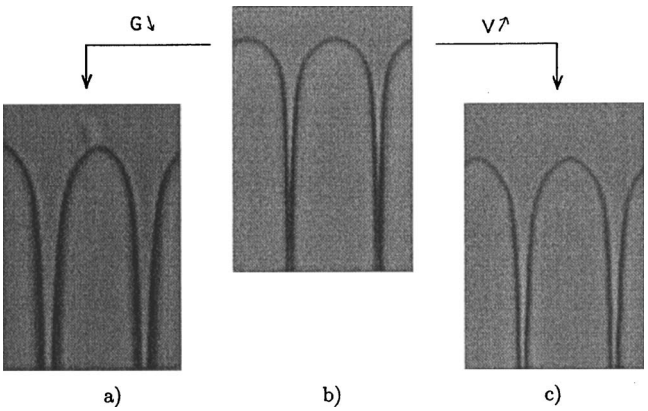

FIG. 5. Cell geometry at $\Lambda\approx 90\ \mu\mathrm{m}$. Evolution with gradient at fixed velocity [(a) to (b)], and with velocity at fixed gradient [(b) to (c)]. Increasing gradient flattens tip cell. Increasing velocity sharpens tip cell. Decreasing gradient from $140\ \mathrm{K\ cm^{-1}}$ to $78\ \mathrm{K\ cm^{-1}}$ then shows similar effect on cell form than increasing velocity from $V=12\ \mu\mathrm{m\ s^{-1}}$ to $V=24\ \mu\mathrm{m\ s^{-1}}$. (a) $(V,\Lambda,G)=(12,95,78)\times(\mu\mathrm{m\ s^{-1}},\mu\mathrm{m},\mathrm{K\ cm^{-1}})$, (b) $(V,\Lambda,G)=(12,90,140)(\mu\mathrm{m\ s^{-1}},\mu\mathrm{m},\mathrm{K\ cm^{-1}})$, (c) $(V,\Lambda,G)=(24,90,140)=(\mu\mathrm{m\ s^{-1}},\mu\mathrm{m},\mathrm{K\ cm^{-1}})$.

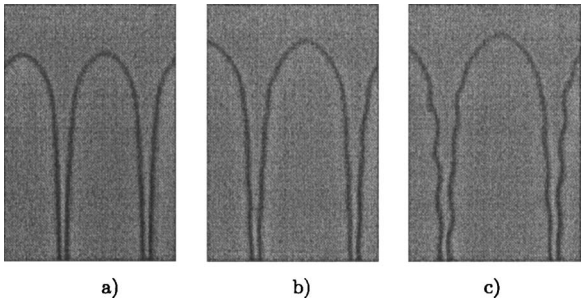

FIG. 6. Evolution of cell form with cell spacing at fixed velocity and thermal gradient: $V=20\ \mu\mathrm{m\ s^{-1}}, G=140\ \mathrm{K\ cm^{-1}}$. (a) $\Lambda=85\ \mu\mathrm{m}$; (b) $\Lambda=100\ \mu\mathrm{m}$; (c) $\Lambda=115\ \mu\mathrm{m}$. Increasing cell spacing yields from the cellular domain (a) to the moderately dendritic domain (c) by crossing marginal states regarding sidebranching (b). (a) $(V,\Lambda,G)=(20,85,140)$ $(\mu\mathrm{m\ s^{-1}},\mu\mathrm{m},\mathrm{K\ cm^{-1}})$; (b) $(V,\Lambda,G)=(20,100,140)$ $(\mu\mathrm{m\ s^{-1}},\mu\mathrm{m},\mathrm{K\ cm^{-1}})$; (c) $(V,\Lambda,G)=(20,115,140)$ $(\mu\mathrm{m\ s^{-1}},\mu\mathrm{m},\mathrm{K\ cm^{-1}})$.

induced inhomogeneities can be considered to have died out before each solidification run.

Cell steadiness is achieved when the concentration field around the cell interface satisfies an advection-diffusion equilibrium. The characteristic time of this process is the advection-diffusion time $\tau_D=l_D^2/D=D/V^2$. However, as the cell interface is a free boundary, its slow evolution toward steadiness implies a change of its undercooling that must be taken into account. Then, the characteristic time toward shape equilibrium gets larger. An estimation of its order of magnitude may be given by the period T of the coupled evolution of cell shape and tip position that is displayed in the $2\lambda-O$ oscillatory instability [15]. This time-scale, which actually corresponds to the longest one evidenced in the present system, has been measured in the same mixture. Together with τ_D, it enables us to evaluate the relevance of our waiting times.

Each study has been performed on cells that were maintained at fixed velocity for long times: at least $45\tau_D\approx 8$ T for $V=8\ \mu\mathrm{m\ s^{-1}}$ and up to $250\tau_D\approx 27$ T for $V=24\ \mu\mathrm{m\ s^{-1}}$. In practice, following a change of velocity, cells evolved but eventually displayed steadiness over most of the observation period. In particular, the length of steadiness extended at least over $20\tau_D$, i.e., 3.5 T. This ensures that all observed cells actually reached a significant state of steadiness.

In the deep cell regime investigated here, uniformity of cell spacing along the front is naturally obtained by phase diffusion beyond a sufficient waiting time based on relevant characteristic times and initial conditions [14]. In practice, observation reveals that, above a dozen of diffusion time scales D/V^2, cell spacing uniformity over the domain under study is achieved. Then, moderate changes of velocity preserve it insofar as instabilities are avoided.

Although most steady states have been obtained from a previous one by slight variations of control parameters, instabilities were sometimes triggered in order to induce a change of cell spacing. Then, a larger waiting time than usual was necessary to reach steadiness again. Besides that, another practical mean for selecting thin (thick) cells has consisted in quickly (slowly) raising the pulling velocity over a

noticeable range. Then, combination of dynamical selection and of instabilities led to uniform states over a larger range of available spacings.

D. Representation variables and control parameters

Exploiting the information conveyed in cell shapes requires correlating them to the variables which describe the steady uniform states to which they refer. As in thermodynamics, this calls for identifying a set of variables capable of univocally characterizing the corresponding states. This set certainly includes the following.

Mixture variables: the capillary length d_0, the solute diffusivity D, the partition coefficient k, the melting temperature of pure succinonitrile T_0, and its drop $T_0-T_L=mc_\infty$ in the actual impure mixture.

Growth variables: the thermal gradient G in which the sample is placed and the pulling velocity V at which solidification is forced to proceed in average.

Morphological variables: the space left to the cell in between its neighbors, i.e., the cell spacing Λ.

We shall assume hereafter that these variables are necessary and sufficient for identifying completely the steady states of uniform patterns. They then correspond to the representation variables of the steady uniform states under study. A criterion for the relevance of this assumption will consist of the coherence of the evolution of data with variables since no coherence can be obtained with superfluous or lacking variable.

Among the representation variables, the morphological variable, i.e. the cell spacing, is unusual since it has long been considered as dependent on the remaining variables, especially the pulling velocity V and the thermal gradient G. This is actually wrong since, for the same mixture variables and growth variables (V,G), a continuous range of cell spacing Λ can be achieved on steady uniform states (Fig. 11). This means that cell spacing must be considered as an additional variable of cell states, not prescribed by the others. Retaining it in the present study is then mandatory since cell spacing obviously parametrizes cell shapes.

In practice, representation variables do not have all the same status. Mixture variables (d_0,D,k,m,c_∞,T_0) are usually fixed insofar as the nature of the dominant impurity and its concentration c_∞ are kept constant. This is the case here since the same mixture has been used at low enough temperatures (below 100 °C) and on short enough cumulative times (about one day) for preventing chemical or thermal dissociation [14]. Accordingly, we shall omit referring explicitly to them in the following. On the opposite, as V and G are changed as desired by experimentalists, we shall call them control parameters. The last variable, Λ, is somewhat specific since it can be changed in the available cell range but by a procedure which do not enable a direct monitoring. The important thing, however, is that scanning different growth histories gives access to all the available desired values. For this reason, we shall keep calling it control parameter in the following.

III. METHODOLOGY

A. Issue

Our purpose consists in determining a relevant analytical representation for the collection of cellular shapes displayed in the experiment. This corresponds to projecting the shape library onto a multiparameter family of functions that is *a priori* both unknown and approximate regarding the actual cell shapes. In addition, our goal is not only to determine analytical curves close to our cell shapes, but also to gain relevant informations on the growth system from the way the parameters of the shape function vary with the control parameters of the experiment.

This issue calls for optimizing the choice of a multiparameter function in a suitable framework. Here the term "suitable" means that the definition of the analytical form of the family of functions and the nature and the number of its parameters are essential for reaching a significant representation of the cell shape library. In particular, the kind of functions retained should involve only nonlinearities that can be physically interpreted and only parameters that are necessary to weight their relative importance. This being satisfied, the evolution of the optimal parameters with the control parameters is likely to convey a physically relevant meaning, provided definite tendencies are displayed.

These concerns are motivated in particular by the fact that analytical optimization of a multiparameter function naturally introduces couplings between the optimal values of each parameters. Following them, different choices of parameters may give forms that approach a given shape equally well. This, together with the slight experimental discrepancies in cell shape observations may then yield large drifts of optimal parameters within the set of equally well fitting parameters. This sensitivity to perturbations would then prevent the emergence of a coherent evolution of a given fit parameter considered separately. A well-known illustration of this issue is given by the fitting of data by power-laws $f(x)=ax^b$. There, in a given bounded domain of x, a *wide* set of couples of parameters (a,b) may give hardly discernable curves. This means that only the selected *couples* of parameters (a,b) can be meaningful, but *none* of their parameters a or b taken solely.

To avoid this difficulty, we shall restrict ourselves to the minimum number of fitting parameters required to describe the variety of physically distinct parts of a cell shape. We shall also take care to consider a range of control parameters wide enough for evidencing definite tendencies in the variations of the fitting parameters.

B. Analysis of cell shapes: relevant cell parts and parameters

Observation of cell shapes shows a curved region at the cell tip, a flat region at the cell grooves, and a matching region in between [Fig. 7(a)]. These regions have long been identified in literature as region I, region III, and region II, respectively [16]. Notice that regions I and III rely on well defined parameters, respectively, the curvature radius at cell tip ρ and the width L of the solid phase channel. On the opposite, the transition region II involves no specific geometrical feature that could be easily taken as a reference for the whole shape. Accordingly, whereas the three parameters ρ,L,Λ do appear necessary to convey the geometric features of the form, the definition of an additional parameter seems physically more obscure. For this reason, we shall only retain

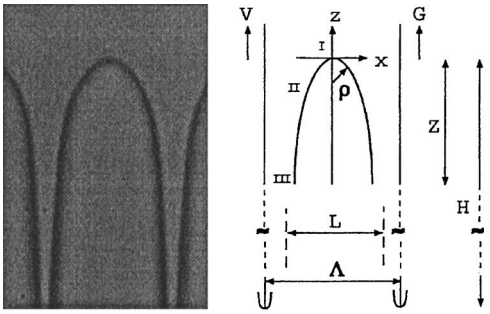

FIG. 7. Typical image of cell (a) and definition of the geometrical axis, the set of variables, and the different cell regions used to study it (b). The cell corresponds to $(V,\Lambda,G)=(12,110,78)$ $(\mu\mathrm{m\,s}^{-1},\mu\mathrm{m},\mathrm{K\,cm}^{-1})$. Variables ρ, L, Λ, Z, and H denote tip curvature radius, cell width, cell spacing, height of the observation window, and groove height. The cell width refers to the apparent asymptotes of cell grooves as seen from the observation window of length Z. Regions I, III, and II refer to cell tip, cell groove, and the matching region in between. Observation directly provides the cell spacing Λ and the window height Z. Fitting gives the curvature radius ρ and the cell width L. The actual groove height remains indeterminate.

the three morphological parameters ρ, L and Λ for fitting the cell shape. In addition to them, the cell length H from cell tip to the end of cell grooves parameterizes, beyond the actual observation window, the height of the whole cell domain.

Notice that, in the low or large Péclet number limit, $Pe \ll 1$ or $Pe \gg 1$, theoretical analyses restrict the possible choices of optimization functions to a one-parameter family. In particular, at large Péclet number, $Pe \gg 1$, where the diffusive scale l_D is small compared to cell spacings $\Lambda, l_D \ll \Lambda$, the impurity concentration field behaves as if the cell was isolated in an infinite medium. Then, as in free growth, equilibrium between advection and diffusion points to a paraboliclike profile for the cell tip [3], to an Ivantsov-like paraboloid [1], parameterized by the curvature radius ρ at cell tip:

$$z = \frac{x^2}{2\rho}. \tag{1}$$

However, this scale-invariant form fails to handle the limits of the cell geometry, i.e. the asymptotic width L of the solid phase. On the other hand, at low Péclet number, $Pe \ll 1$, the diffusion scale englobes many cells: $\Lambda \ll l_D$. Diffusion is thus the dominant phenomenon to set a cell shape compatible with the prescribed cell boundaries. For steady cells, the interface shape then satisfies a geometry analogous to that found in viscous fingering [2], i.e., a Saffman-Taylor-like geometry parametrized by the relative finger width λ [17]:

$$\pi\frac{x}{\Lambda} = \lambda \arccos\left[\exp\left(\frac{\pi}{1-\lambda}\frac{z}{\Lambda}\right)\right]. \tag{2}$$

However, as this corresponds to a one-parameter family of forms, the relative tip curvature radius $\tilde{\rho}=\rho/\Lambda$ is then prescribed by the relative cell width $\tilde{L}=L/\Lambda$: $\tilde{\rho}\equiv\tilde{\rho}(\tilde{L})$. On the opposite, in the present intermediate Péclet number regime $Pe=O(1)$, at least *two* independent nondimensional parameters, e.g., $(\tilde{\rho},\tilde{\Lambda})$, are *a priori* required to model the cell shape. Accordingly, the dimensional fitting functions will involve the three lengths (ρ,L,Λ) as geometrical parameters.

C. Global optimization

We seek a family of functions $f_{\rho,L,\Lambda}(\cdot)$ parametrized by the tip curvature radius ρ, the solid phase width L, and the cell spacing Λ, which could be capable of accurately fitting the whole cell shape. We shall be guided in this by several requirements that are reported below. Once the family of fitting functions is chosen, the optimal function will be determined first on each cell by an *individual* optimization, i.e., a fitting procedure, and then on the family of cells by a *collective* optimization of the way the fit parameters (ρ,L,Λ) vary with the control parameters (V,Λ,G).

1. Individual optimization

We first assume a fit function at least twice differentiable everywhere. Although this property is required for the existence of a curvature radius, it may be invalid in crystal growth as shown by the joint theoretical [18,19] and experimental [20] determination of the shape of the 3D freely growing xenon dendrite: $z \sim x^{5/3}$ in the frame (x,z) taken with an origin at the dendrite tip. Here, we shall assume that thermal gradient or the presence of neighboring cells regularize such curvature singularity at the tips.

We then notice that the grooves actually vanish at a large but *finite* distance H from the tip [Fig. 7(b)] so that this length should *a priori* parametrize the fitting function. However, as the groove end stands far beyond the height Z of the window within which the cell is studied, $H \gg Z$, groove vanishing can hardly be anticipated from the sole observations of the cell in this window (Fig. 7). Thanks to this, we shall assume that the observed part of the cell behaves as if the groove width remained constant in the asymptotic limit $z \to \infty$: $\lim_{z\to\infty} f_{\rho,L,\Lambda}(z)=L$. This turns out assuming that the length $H-Z$ of the matching zone between the groove ends and the apparent asymptotes of the cell sides is of no importance for the observed cell form (Fig. 7).

The way the cell interface approaches its asymptotes in the long groove limit is set by the Scheil equation. For a miscibility gap $\Delta c=(T_L-T_S)/m$ varying linearly with the impurity concentration c_∞, the distance to the asymptote decreases algebraically as a power law; for a constant miscibility gap, it decreases exponentially. In the present experiment, the miscibility gap varies linearly with concentration but the observed asymptotes at $x=\pm L$ are only virtual since the interface does actually reach the cell boundaries $x=\pm\Lambda$ at $z=-H$ beyond the observation window (Fig. 7). This in particular means that the Scheil domain likely stands beyond the observed asymptotes so that no definite tendency, algebraic or exponential, has to be imposed to the way the observed interface approaches them.

The present issue thus involves a number of characteristic lengths $(\rho,L,\Lambda,l_D,l_T,d_0)$ among which one of them can be taken as a gauge for nondimensionalizing the others. We

choose the cell spacing Λ as this standard length and we note nondimensional lengths with a tilde: $\tilde{x}=x/\Lambda$, $\tilde{z}=z/\Lambda$, $\tilde{\rho}=\rho/\Lambda$ and $\tilde{L}=L/\Lambda$. This yields us to seek functions $f_{\tilde{\rho},\tilde{L}}(.)$ relying the interface data points $(\tilde{x}_i,\tilde{z}_i)_{i=1,\ldots,N}$:

$$\tilde{x}_i = f_{\tilde{\rho},\tilde{L}}(\tilde{z}_i). \tag{3}$$

Taking the mean interface direction x as the ordinate and the cell axis z as the abscissa provides horizontal asymptotes that are much easier to fit to a good accuracy with a usual fitting procedure than vertical asymptotes [Fig. 2(c)]. To avoid bivalued graphs, a reflexion of the upper branch, $x>0$, $z<0$ onto the $x>0$, $z>0$ domain is applied: $z\to -z$ for $x>0$ [Fig. 2(d)]. In this framework, requiring that ρ and L correspond to tip curvature radius and to cell width implies:

$$f_{\tilde{\rho},\tilde{L}}(\tilde{z}) \sim_{\tilde{z}\to 0} \mathrm{sgn}(\tilde{z})\sqrt{2\tilde{\rho}|\tilde{z}|}, \tag{4}$$

$$\lim_{\tilde{z}\to\pm\infty} f_{\tilde{\rho},\tilde{L}}(\tilde{z}) = \mathrm{sgn}(\tilde{z})\frac{\tilde{L}}{2}. \tag{5}$$

These constraints nevertheless allow for a large variety of test functions, most of which are incompatible with an accurate fitting of region II.

The search for suitable fitting functions has been performed on generating functions $g(\cdot)$ defined this way:

$$f_{\tilde{\rho},\tilde{L},n}(\tilde{z}) = \mathrm{sgn}(\tilde{z})\frac{\tilde{L}}{2} g^n(\zeta^{1/2n}), \tag{6}$$

$$\zeta = 2\tilde{\rho}|\tilde{z}|(\tilde{L}/2)^{-2}, \tag{7}$$

where n is an additional real parameter and where $g(\cdot)$ is a C^2 function which involves an asymptotic limit of 1 and which vanishes at the origin with a derivative equal to unity. In the present study, attention has been restricted to the following functions:

$$g(s) = \tanh(s), \tag{8}$$

$$g(s) = \frac{2}{\pi}\arctan\left[\frac{\pi}{2}s\right], \tag{9}$$

$$g(s) = 1-\exp(-s). \tag{10}$$

Each of these $g(\cdot)$ functions has been used to fit each of the shapes of the cell library. Soon in the fitting process, the generating function (8) has been recognized as giving more satisfactory fits than the two others (Sec. IV A). It has thus been selected to proceed for the search for a geometrical representation of cell shapes. Fitting each cell then gave the value of the optimal fit parameters $(\tilde{\rho},\tilde{L},n)$ at each triplet of control parameters (V,Λ,G).

2. Collective optimization

The individual optimization has further been extended to a collective optimization by fitting the fit parameters $(\tilde{\rho},\tilde{L},n)$ with the control parameters (V,Λ,G) using power laws (Sec. IV B). However, analysis of the variation of exponent n showed incoherent evolutions with V and G and a large coupling with the other fit parameter $\tilde{L}$. For these reasons, n has been fixed to definite values for which new optimal values of $(\tilde{\rho},\tilde{L})$ have then been determined.

The collective optimization turned out to extract the dominant tendency of the variation of the fit parameters with the control parameters. This determination has even been made simpler by rounding the values of the exponents of the power laws. In all cases, the resulting two-parameter function $f_{\tilde{\rho},\tilde{L},n}(\cdot)$ with fixed n and variable $\tilde{\rho}\equiv\tilde{\rho}(V,\Lambda,G)$ and $\tilde{L}\equiv\tilde{L}(V,\Lambda,G)$ has been checked against cell shape so as to validate the overall procedure.

Altogether, these results provide a definite analytical representation of cell shapes with respect to the control parameters (V,Λ,G) (Sec. V) in a way that allows physical interpretation of shape evolution with respect to them (Sec. VI).

IV. GLOBAL DETERMINATION OF CELL SHAPE

A. Individual optimization

We address the optimal determination of the shape of definite cells, either steady or moderately dendritic. For this, we fit each observed cell by the three functions (8)–(10) with fitting parameters $(\tilde{\rho},\tilde{L},n)$.

Figure 8 compares, for a given cell, the optimal fits obtained for these three functions. It appears that all of them fit this cell quite satisfactorily [Fig. 8(a)]. In particular, enlargements of definite regions [cell tip, cell groove, and in between, Figs. 8(b)–8(d)] reveal a mismatch between fits and data that is smaller than data resolution. Accordingly, none of these fit functions are to be eliminated from comparison with this definite cell and more generally from comparison with any other.

That different functions fit a given form equally well may be surprising at first glance. This however results from the fact that they all involve here asymptotes and a parabolic shape at the tip that are adjusted to data by definite parameters, ρ and L. Accordingly, deviations from experimental profiles can only occur at the third order in the transition region between tip and grooves or within the asymptotic decay toward the asymptotes. The former effect is weak since the transition region is finite and the latter effect is rendered below the resolution by adjustment of parameter L. All functions therefore provide an accurate fit to data, the noticeable differences between their asymptotic tendencies being rejected in practice beyond the observation window.

Turning attention to the fit results over the cell library, we observe that, in average, the exponential function (10) provides slightly weaker fit quality factors. For this reason, we shall focus attention on the remaining functions $g(s)=\tanh(s)$ (8) and $g(s)=2/\pi\ \arctan[\pi/2s]$ (9). It then appears that, in average over the cell library, they, respectively, yield $\tilde{L}=0.9<1$ and $\tilde{L}=1.15>1$. The latter value is incoherent since, by definition, the solid phase width L must be smaller than the cell spacing Λ: $\tilde{L}<1$ [Fig. 7(b)]. This means that for function (9) the infinite groove limit $H\to\infty$ is singular since

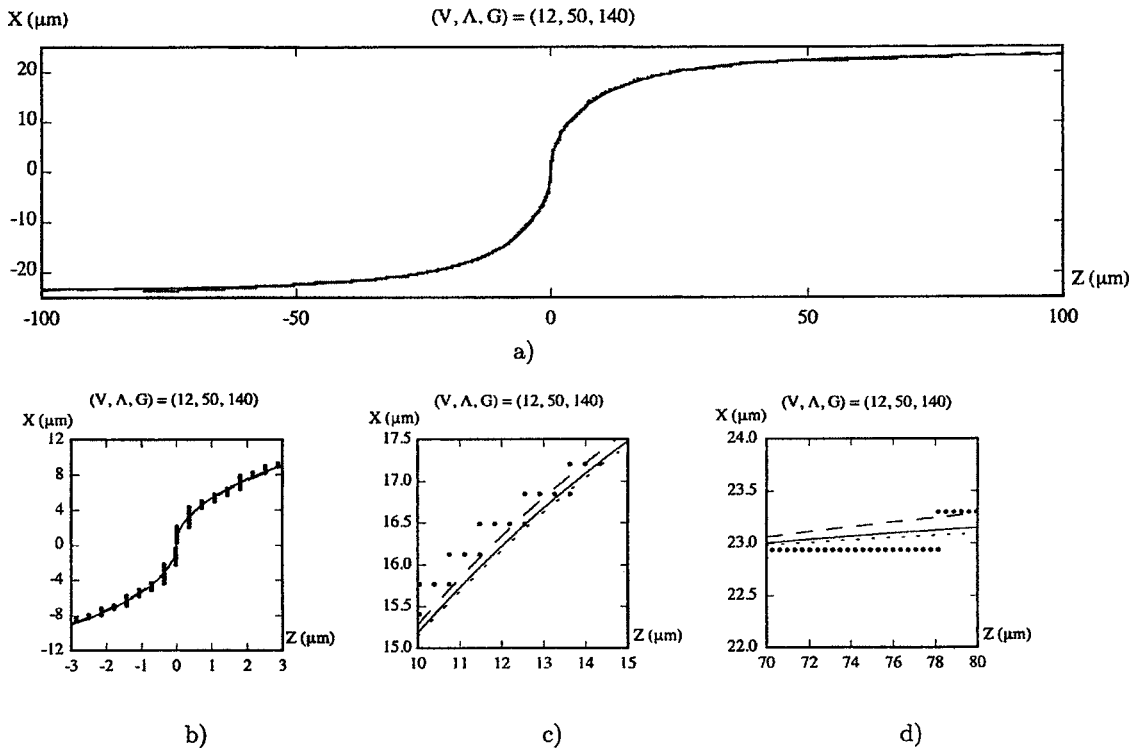

FIG. 8. Optimal fits of a given cell by the three functions (8), (9), and (10). Dots correspond to data and full line, large dashed line, and short dashed line to fits by functions (8), (9), and (10), respectively. The cell corresponds to $(V,\Lambda,G)=(12,50,140)$ (μm s^{-1}, μm, K cm^{-1}) and the fit results are $(\rho,L,n)=(14.5,46.9,0.82)$ for function (8), $(\rho,L,n)=(13.5,49.8,0.52)$ for function (9), and $(\rho,L,n)=(15.1,46.5,0.51)$ for function (10). (a) Full cell. (b) Enlargement of cell tip (region I). (c) Enlargement of the transition region (region II). (d) Enlargement of the asymptote (region III). All functions (8), (9), and (10) fit the cell equally well but the average of the fit quality factors over the cell library is slightly smaller for function (10). One also notices that parameter L is close to Λ for function (9) here and is actually larger in average over the cell library: $L=1.15\Lambda$. Both statements lead us to privilege function (8) for representing shapes over the cell library.

the degenerate problem $H=\infty$ provides a solution that is meaningless. This leads us to privilege function (8), $g(s)=\tanh(s)$, for seeking a meaningful representation of cell geometry.

B. Collective optimization

When scanning the cell library, all the optimal fitting parameters $(\tilde{\rho},\tilde{L},n)$ referring to function (8) vary. Each of these triplets indicates the best values found for accurately reproducing a definite cell shape. This, however, does not correspond to a sharp selection of the fitting parameters taken separately since, usually, other triplets can also fit the given shape nearly equally well (see Sec. III A). This follows from the fact that, in the vicinity of a triplet $p=(\tilde{\rho},\tilde{L},n)$, other triplets $p+\delta p$ will provide close values of function $f_{\tilde{\rho},\tilde{L},n}(z)$ insofar as δp belongs to the plane normal to $\nabla_p f(z)$ where $\nabla_p=(\partial/\partial\tilde{\rho},\partial/\partial\tilde{L},\partial/\partial n)$: $\delta f_{\tilde{\rho},\tilde{L},n}(z)=\delta p.\nabla_p f(z)=0$. Although this cannot be satisfied at any z by a given δp, this means that, in average, a bounded two-dimensional surface of parameters actually fit almost equally well a given data set. Accordingly, spurious variation of each parameter can be expected, thereby preventing us from interpreting each of them separately. This, in particular, will be the case for the exponent n (Figs. 9 and 10) and, accordingly, for the other fit parameters determined for a freely varying n.

To palliate this caveat, we seek to reduce the number of fit parameters so as to eliminate the incoherent component of their variations from one cell to the other. For this, we fix one of the fit parameters and extract the averaged evolution of the two remaining ones with control parameters (V,Λ,G). However, whereas fixing parameters n or $\tilde{L}$ to a definite value can be compatible with data, fixing $\tilde{\rho}$ cannot since $\tilde{\rho}$ largely varies on cell library (see cell forms on Figs. 3–6 and data variations in Figs. 9 and 10). Accordingly, we shall restrict ourselves to exploring the implications of fixing n or $\tilde{L}$ in the following.

The simplest way of fixing the width of the solid phase L to an objective value turns out to set it at the cell spacing value: $L=\Lambda$, i.e., $\tilde{L}=1$. This corresponds to placing the asymptotes of the fit function at the cell boundaries and, thus, to denying the existence of grooves in the asymptotic limit $z\to\infty$, as is actually the case in practice. However, whereas disappearance of grooves actually occurs in practice far from the boundaries of the observation windows, $\tilde{H}\gg 1$, placing it at infinity turns out assuming here that the limit $\tilde{H}\to\infty$ is regular in the present instance.

The status of exponent n is special in that it monitors the nature of the nonlinearity of cell geometry. In particular,

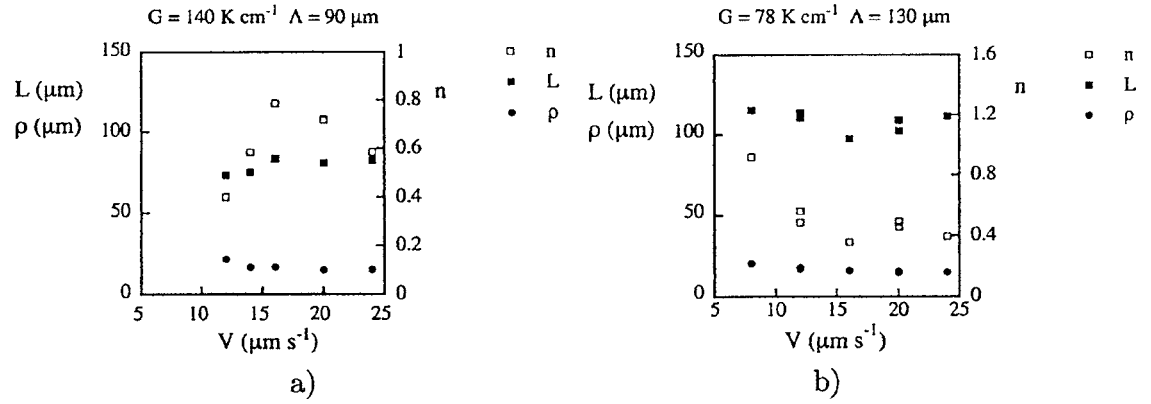

FIG. 9. Typical variations of exponent n, solid phase width L, and curvature radius ρ with V at fixed Λ and G. (a) $G=140$ K cm^{-1}; $\Lambda=90$ μm. (b) $G=78$ K cm^{-1}; $\Lambda=130$ μm.

changing it mimics a change of branch of solution, a thing that cannot reasonably occur several times within our moderate scale range. Accordingly, we shall find it more relevant to restrict the analysis to a definite kind of nonlinearity, i.e., a definite n, that will be either naturally given by the fit results or imposed by fixing n in specific domains.

On the other hand, directional solidification is based on largely separated length scales, $d_0 \approx 10^{-2}$ μm, $l_D \approx 10^2$ μm, $l_T \approx 10^3$ μm, whose values nondimensionalized by $\Lambda \approx 10^2$ μm amount to $\tilde{d}_0 \approx 10^{-4}, \tilde{l}_D \approx 1, \tilde{l}_T \approx 10$. Accordingly, the nondimensional morphological scales $\tilde{\rho}$ and $\tilde{L}$ may be viewed as combinations of small ($\tilde{d}_0$), moderate ($\tilde{l}_D$), and large ($\tilde{l}_T$) numbers. For this reason, one expects them to express as a multiplicative algebra rather than as an additive algebra of these variables, i.e., in terms of power laws of $(\tilde{d}_0, \tilde{l}_D, \tilde{l}_T)$ or, equivalently, of (V, Λ, G). In practice, we shall consider power law variations of ρ, L, and $\Lambda - L$:

$$\rho = c_\rho V^{e_V} \Lambda^{e_\Lambda} G^{e_G}, \tag{11}$$

$$L = c_L V^{f_V} \Lambda^{f_\Lambda} G^{f_G}, \tag{12}$$

$$\Lambda - L = c_{\Lambda - L} V^{g_V} \Lambda^{g_\Lambda} G^{g_G}. \tag{13}$$

As the cell width L can only be positive and smaller than the cell spacing $\Lambda, 0 < L < \Lambda$, the representations (12) and (13) are limited to bounded ranges in practice. In particular, relations (12) and (13) will appear not to apply above and below a velocity bound respectively. Altogether, they will be useful however to extrapolate our findings beyond the present experimental range. Although they are equivalent in this range up to experimental uncertainty, it will appear more convenient in the following to use relation (12) instead of (13) to discuss the main features and implications of cell form evolution. This is why we shall report in the following in more detail the way it has been determined.

The above statement implicitly considers the fluctuations of ρ or L with control parameters that are not linked to a general trend as spurious consequences of a coupling between fit variations. We shall then seek to reduce them by appropriately fixing a fit parameter.

The details of the procedure applied for this collective optimization is reported in the Appendix. It led us to let ρ and L freely vary but to fix n to a definite value, $n=0.5$ or $n=1$. On the other hand, three domains have been distinguished for extracting power laws from the parameter varia-

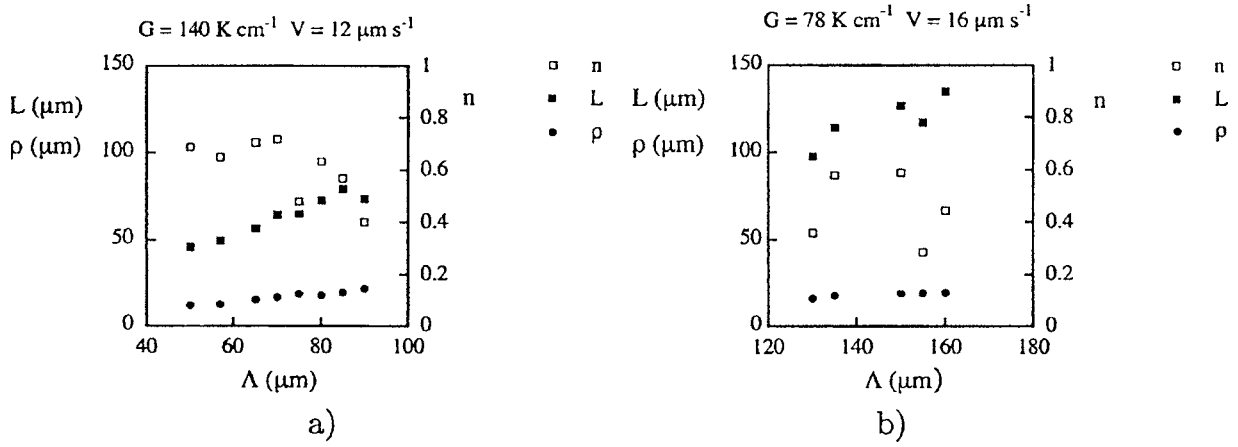

FIG. 10. Typical variations of exponent n, solid phase width L, and curvature radius ρ with Λ at fixed G and V. (a) $G=140$ K cm^{-1}; $V=12$ μm s^{-1}. (b) $G=78$ K cm^{-1}; $V=16$ μm s^{-1}.

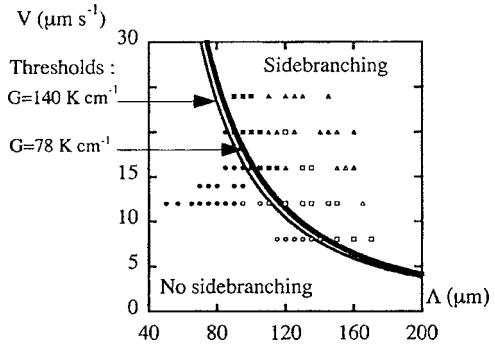

FIG. 11. Representation of the states composing the cell library in the (V,Λ) space. Full symbols refer to thermal gradient $G=140$ K cm^{-1}, $V_c=4$ μm s^{-1} and open symbols to $G=78$ K cm^{-1}, $V_c=2$ μm s^{-1}. Circles, squares, and triangles, respectively, refer to steady cells, weak sidebranching, and moderate sidebranching.

tions: the steady cell or weakly dendritic domain [Figs. 12(a) and 12(b)], the moderately dendritic domain [Fig. 12(c)] and their merge. These are displayed in Fig. 11 where all the states observed in this study are reported.

The first domain includes the weakly dendritic forms that are displayed in the vicinity of the sidebanching transition [Fig. 12(b)]. They correspond to sidebranch amplitudes A small compared to the cell spacing Λ: $A<\Lambda/20$. In comparison, the moderately dendritic domain is defined by $\Lambda/20<A<\Lambda/10$ (Sec. II B). Merging the pure steady cell domain and the weak sidebranching domain has been found convenient to enhance the quality of the fits by enlarging the range of variables (V,G) and the data number. Its relevance will be legitimized by the absence of transition in the fit results at the occurrence of sidebranching.

The results of the fits are exemplified in Fig. 12 on three different kinds of cells: a steady cell [Fig. 12(a)] a weakly dendritic cell [Fig. 12(b)] and a moderately dendritic cell [Fig. 12(c)]. For all of them, the forms reconstructed from (6) with generating function $g(s)=\tanh(s)$ (8) and $n=0.5$ are plotted. We have not plotted the forms obtained with exponent $n=1$ since they are hardly discernable from those obtained at $n=1/2$ with the naked eye. However, the quality factor of the fits indicate that fitting with $n=0.5$ is more accurate than fitting with $n=1$. For this reason, we shall retain from now on the value $n=1/2$ for exponent n.

C. Validation

Table I reports the prefactors and exponents found for ρ and Λ in the various regimes considered here and for $n=1/2$. Interestingly, fitting on the steady or weakly dendritic domain gives exponents that are close to those obtained on the moderately dendritic regime or on the whole data domain. Thanks to this homogeneity of the fit results in the cell library, we shall consider the fit on the whole data domain as relevant for cell shapes in the cellular to moderately dendritic regime. In addition, in order to facilitate the interpretation of the shape determination, we shall consider the values of the exponents rounded to 10% and the corresponding recomputed prefactors:

$$c_\rho = 0.095 \times 10^2\ \mu\text{m s}^{-1/4}\,\text{K}^{-1/2},$$
$$e_V = -\frac{1}{4}, \quad e_\Lambda = \frac{3}{4}, \quad e_G = \frac{1}{2}, \tag{14}$$

$$c_L = 0.66 \times \mu\text{m}^{-1/10}\,\text{s}^{1/10}, \quad f_V = \frac{1}{10}, \quad f_\Lambda = 1, \quad f_G = 0. \tag{15}$$

In comparison, the exponents and prefactors of the power law (13) relevant to $\Lambda - L$ read:

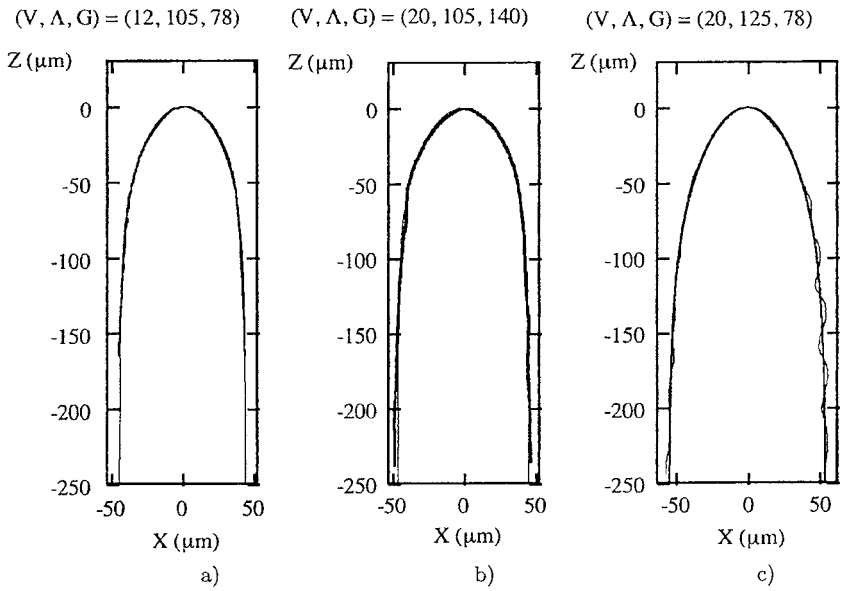

FIG. 12. Comparison between the actual cell shapes (heavy lines) and those reconstructed from (6) with generating function $g(s)=\tanh(s)$ (8), $n=0.5$ and rounded parameters (14) and (15) (light lines). Using the optimal parameters ρ and L instead of the rounded values would yield forms not distinguishable with the naked eye from those actually plotted. (a) $(V,\Lambda,G)=(12,105,78)$ (μm s^{-1}, μm, K cm^{-1}); (b) $(V,\Lambda,G)=(20,105,140)$($\mu$m s^{-1}, μm, K cm^{-1}); (c) $(V,\Lambda,G)=(20,125,78)$($\mu$m s^{-1}, μm, K cm^{-1}).

TABLE I. Tables correspond to fit results with generating function (8) and $n=1/2$. They report the prefactors and the exponents of the power law variations (11) and (12) of the fit parameters ρ and L in the three kinds of domains: steady or weakly dendritic domain, the moderately dendritic domain, and the whole domain. The last column indicates the rounded values of the exponents on the whole domain and the corresponding prefactors.

ρ	Steady or weakly dendritic	Moderately dendritic	Whole library	Rounded values
c_ρ	0.073	0.040	0.0747	0.095
e_V	−0.25	−0.2	−0.25	−1/4
e_Λ	0.8	1	0.85	3/4
e_G	0.5	0.4	0.45	1/2
L	Steady or weakly dendritic	Moderately dendritic	Whole library	Rounded values
c_L	0.828	0.255	0.655	0.66
f_V	0.1	0.1	0.1	1/10
f_Λ	0.95	1.1	1.0	1
f_G	0	0.1	0	0

$$c_{\Lambda-L}=1.21, \quad g_V=-0.55, \quad g_\Lambda=1.1, \quad g_G=-0.25. \tag{16}$$

They yield values of cell widths L which, in the present experimental range and to the experimental uncertainty, are identical to those given by (12) and (15). Notice that, as $\Lambda - L$ is about a tenth of Λ, relation (13) turns out fitting L at the next order in Λ compared to relation (12). This is why the corresponding exponents show so little correlation.

To validate the result of the collective optimization, we now compare the observed forms with those reconstructed by the fit (6) and (8) with parameters corresponding to relations (14) and (15). Figure 12 reveals quite a good agreement for steady cells [Fig. 12(a)] or weakly dendritic cells [Fig. 12(b)], the distance from fits to data being less than five pixels. Encouraged by this agreement, we extrapolate the analytical representation of cells to the moderately dendritic regime. As shown in Fig. 12(c), the analytical form here too satisfactorily reproduces the actual shapes of the growth forms. In particular, the dendrite tip is accurately reproduced and the analytical curves of mean shapes lay well within the bumps of the dendrite sides.

V. CELL EVOLUTION WITH CONTROL PARAMETERS

The evolution of cells with control parameters involves both the evolution of their position in the thermal field, i.e., equivalently the cell tip undercooling, and the evolution of their shape from their tip to their grooves.

Cell tip undercooling Δ_t has been accurately determined in a previous experimental study for the same mixture and in the same setup [5]. It appeared to evolve according to the Brody-Bower-Flemings criterion [21]:

$$\Delta_t = \frac{V_c}{V}, \tag{17}$$

where Δ_t denotes the relative position z_t of cell tip in the thermal gradient, in between the positions of the solidus line z_S and of the liquidus line z_L:

$$\Delta_t = \frac{z_L - z_t}{z_L - z_S}. \tag{18}$$

These positions (z_S, z_L) at the nominal solutal concentration c_∞ of the mixture are set by thermodynamical relationships. In particular, their distance reads: $z_L - z_S = D/V_c = l_T$. This, together with (17) and (18), provides the localization of cell tips:

$$z_L - z_t = D/V = l_D. \tag{19}$$

On the other hand, the present study has provided a simple global analytical determination of the shape library following which, for given control parameters (V, Λ, G), the cell geometry $x(z)$ satisfies:

$$x = \frac{L}{2}\tanh^{1/2}\left[8\frac{\rho z}{L^2}\right] \tag{20}$$

with ρ and L given by power laws (11) and (12) with prefactors and exponents (14) and (15). This parametrization provides an implicit determination of the function $x = F_{(V,\Lambda,G)}(z)$ that describes the cell geometry (x,z) in the control parameter space.

Taken together, the determinations (17), (18), and (20) provide a complete determination of cells, both in position and shape, and for any control parameters. They thus give us the opportunity of easily addressing the evolution of the growth solution with control parameters at *fixed* solutal concentration c_∞.

A. Single parameter variation

The effects on cell shape of the variation of a *single* control parameter, V, Λ, or G, are illustrated in Fig. 13. It is found that increasing either V [Fig. 13(a)] or Λ [Fig. 13(b)] sharpens cell tips but that increasing G [Fig. 13(c)] makes them rounder. As the sharpness of cell tip refers to the reduced curvature radius ρ/L, this tendency is consistent with

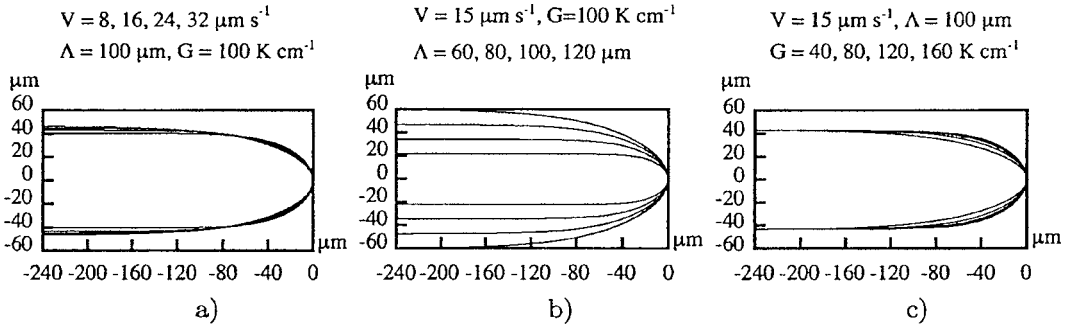

FIG. 13. Evolution of cell shape with (a) pulling velocity V: $V=8,16,24,32\ \mu\mathrm{m\,s^{-1}}$ with $\Lambda=100\ \mu$m and $G=100\ \mathrm{K\,cm^{-1}}$; (b) cell spacing Λ: $\Lambda=60,80,100,120\ \mu$m with $V=15\ \mu\mathrm{m\,s^{-1}}$ and $G=100\ \mathrm{K\,cm^{-1}}$; (c) thermal gradient G: $G=40,60,80,100\ \mathrm{K\,cm^{-1}}$ with $V=15\ \mu\mathrm{m\,s^{-1}}$ and $\Lambda=100\ \mu$m. In figures (a) and (c), cell tip position in the thermal gradient varies from cell to cell. To allow an easy comparison of their shapes, they have been translated so as to display the same apparent tip position.

the scaling laws (11), (12), (14), and (15) following which:

$$\frac{\rho}{L}=0.144\ V^{-0.35}\Lambda^{-1/4}G^{1/2}. \tag{21}$$

In particular, small ρ/L, i.e., large V, Λ, or $1/G$ means sharp cell tips, as displayed in Fig. 13.

B. Combined parameter variations

Combined variations of the control parameters (V,Λ,G) enable modifications of cell spacing (Λ), cell shape (ρ/Λ), and cell position in the thermal field $(z_L-z_t=l_D)$ at the *same* nominal solutal concentration c_∞. Interestingly, as the relationship between the control parameter space $\{\Lambda,V,G\}$ and the spacing-shape-position space $\{\Lambda,\rho/\Lambda,z_L-z_t\}$ $\propto\{\Lambda,V^{-1/4}\Lambda^{-1/4}G^{1/2},V^{-1}\}$ is bijective, *any* choice of cell spacing, cell shape and cell position can be achieved by suitably selecting the control parameters. This means in particular that cell position, cell spacing and cell shape are three *independent* features of growth cells that can be set independently one of the other.

To illustrate this, we show in Fig. 14(a) that, keeping the cell spacing Λ constant, the *same* shape can be found either *close* or *far* from the liquidus line. This is achieved by choosing V so as to meet the required distance l_D from the cell tip to the liquidus line and then by adjusting G so that the shape parameter ρ/Λ stay unchanged. Similarly, still for a constant cell spacing Λ, the position of a cell can be made unchanged while its shape gets rounder [Fig. 14(b)]. This is simply obtained by keeping the same V, thus the same distance $z_L-z_t=l_D$ to the liquidus line but by changing the thermal gradient G so as to monitor the change of the shape variable ρ/Λ.

A similar remark can also be made on the usual nondimensional variables, tip undercooling Δ_t, Péclet number Pe, and shape variable ρ/Λ since this triplet is made of variables as independent as the control parameters: $\{\Delta_t,Pe,\rho/\Lambda\}$ $\propto\{G/V,V\Lambda,V^{-1/4}\Lambda^{-1/4}G^{1/2}\}$. Then, keeping the same tip undercooling and the same Péclet number, the cell shape may actually be changed [Fig. 14(c)] by varying G, V, and Λ^{-1} so as to keep G/V and ΛV constant. In the same spirit, the same form can be obtained at the same tip undercooling but at different Péclet numbers [Fig. 14(d)] provided one keeps the same ratio G/V and adjusts Λ so that the shape variable ρ/Λ remains unchanged.

As all these cells refer to steady states, their incoming impurity flux $\Lambda V c_\infty$ must be balanced by the impurity flux absorbed along their interface:

$$\Lambda V c_\infty=\int_I (1-k)c_I\mathbf{V}\cdot\mathbf{n}\,ds, \tag{22}$$

where I denotes the interface, c_I its impurity concentration, and n its normal. This conservation relation helps understanding the relationship between the cell shape and the concentration at the cell tip or equivalently, with the control parameters. In particular, a change of the location of a cell while keeping the same shape is obtained by changing the distance to the liquidus line with V and by recovering the same concentration at the cell tip by varying the position of the solidus line with G. Similarly, changing a cell shape while keeping its distance to the liquidus position is obtained by changing the thermal gradient G but keeping the same velocity V. As the solidus line has moved, the concentration at the cell tip, and thus along the cell interface, has then changed. However, this is counterbalanced by the change of shape so that the net absorbed flux along the interface (22) remains the same.

The relationships (19) and (20) giving the position and the shape of cells can be recast by using the characteristic lengths of directional growth: the cell spacing Λ, the diffusion length $l_D=D/V$, the thermal length $l_T=D/V_c$ and the capillary length d_0. Plugging relations (11) and (12) in (20) yields:

$$z_L-z_t=l_D, \tag{23}$$

$$x=\frac{\Lambda}{2}c_x\left(\frac{l_D}{d_0}\right)^{-1/10}\tanh^{1/2}\left[c_z\left(\frac{l_D}{d_0}\right)^{9/20}\left(\frac{\Lambda}{d_0}\right)^{-1/4}\left(\frac{l_T}{d_0}\right)^{-1/2}\frac{z}{\Lambda}\right], \tag{24}$$

where the nondimensional prefactors c_x and c_z read:

$$c_x=c_L\left(\frac{D}{d_0}\right)^{1/10}, \tag{25}$$

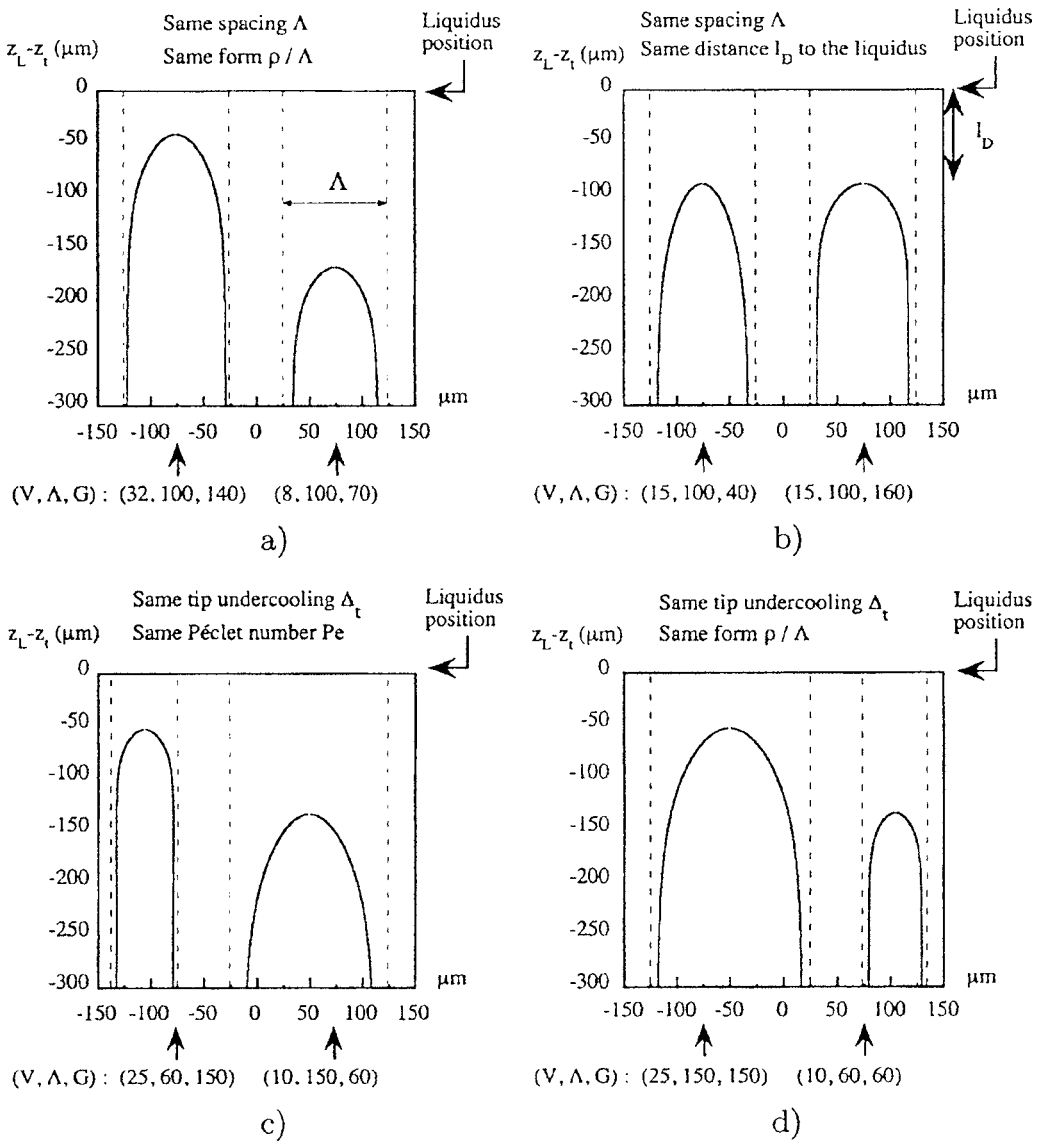

FIG. 14. Evolution with control parameters of cell spacing Λ, cell shape ρ/Λ, and distance of cell tip to the liquidus position $z_L-z_t=l_D=D/V$ with respect to the liquidus line z_L-z_t: (a) same spacing and form but distinct positions (b) same spacing and position but distinct shapes. Evolution with control parameters of cell tip undercooling Δ_t, cell form ρ/Λ, cell spacing Λ, and Péclet number $Pe=\Lambda V/D$: (c) same tip undercooling Δ_t and Péclet number Pe but distinct forms and spacings (d) same tip undercooling Δ_t and form but different Péclet numbers Pe and spacings. Units for (V,Λ,G) are $(\mu\mathrm{m\,s^{-1}},\mu\mathrm{m},\mathrm{K\,cm^{-1}})$.

$$c_z = 8\frac{c_\rho}{c_L^2}(T_L - T_S)^{1/2} d_0^{-3/10} D^{-9/20}, \tag{26}$$

with $c_L=0.66\ \mu\mathrm{m}^{-1/10}\,\mathrm{s}^{1/10}$ (15), $c_\rho=0.095\times 10^2\mu\mathrm{m\ s}^{-1/4}\,\mathrm{K}^{-1/2}$ (14) and $T_L-T_S=m\Delta c$ where $\Delta c=mc_\infty(1-k)/k$ denotes the miscibility gap. Expressed with respect to the Péclet number $Pe=\Lambda V/D$, the reduced pulling velocity $\nu=V/V_c$, and the surface tension parameter $\sigma=d_0 l_T/\Lambda^2$, cell shape then reads:

$$x = \frac{\Lambda}{2} c_x \left(\frac{\sigma Pe^2}{\nu}\right)^{1/10} \tanh^{1/2}\left[c_z \sigma^{3/10} Pe^{7/20} \nu^{-4/5} \frac{z}{\Lambda}\right]. \tag{27}$$

Notice that relations (24) and (27) apply insofar as cell width L is smaller than cell spacing Λ. Otherwise, they must be replaced by relation (20) complemented with power laws (11) and (13).

Determinations (24) and (27) are exhaustive with respect to variables V,Λ,G, but undetermined regarding the impurity concentration c_∞ which was fixed in our experiment. As a result, prefactors c_L and c_ρ can only be given numerically for the particular values of mixture variables used here, whereas they should expressed with respect to these variables to complete the determination. Nevertheless, dimensionality and physical considerations may together provide additional information on the way prefactors vary with variables. Assuming the relevance of the minimal model of solidification, nondimensional prefactors c_x and c_z should express with respect to its variables others than (V,Λ,G), i.e., D,k,m,c_∞,d_0. The only dimensionally correct possibility is

then a dependence on the temperature ratio mc_∞/T_0 and on k. However, physical analysis shows that both variables can only enter the minimal model through the combination $m\Delta c/T_0=(T_L-T_S)/T_0$ so that c_x and c_z can only be a function of them:

$$c_x \equiv c_x\left(\frac{T_L-T_S}{T_0}\right), \quad c_z \equiv c_z\left(\frac{T_L-T_S}{T_0}\right). \tag{28}$$

Note that, in contrast with the set of relevant length scales, the range of variation of $(T_L-T_S)/T_0$ is short in practice. The argumentation supporting power law relationship then does not hold for it.

VI. DISCUSSION

A. Nature of the shape determination

The present determination of cell shapes has addressed cell parts going from the rounded tip region to the nearly flat regions of cell sides. It has thus referred to a largely nonlinear geometry going from a curved domain to asymptotically straight domains. In addition, in these working windows, the cell shape has been fitted not by parts but as a whole.

One of the major advantages of this procedure has been to negligibly depend on extrinsic parameters as the height of the observation window for instance (Fig. 7). This contrasts with fitting procedures that may be used to extract a tip curvature radius from the study of a tip region only. There, the width of the selected tip region is *a priori* of prime importance for the result since the tip region is known to be neither circular, nor parabolic [4,22]. At best, only the window widths for which the sensitivity of the measured tip radius is minimal can yield a relevant result [22]. On the opposite, here, the height Z of the observation window has minute influence on the fit since it only monitors the length of a part of the cell that is nearly straight. Then, the problem of setting out this extrinsic parameter is simply avoided. This is especially interesting for states for which defining a relevant observation window would have been delicate, as when moderate sidebranches are emitted. Here, the relevance of the fitting procedure can be extrapolated to them, thereby providing a rational comparison between steady and moderately dendritic forms on the same basis.

In the present solidification issue, the resulting analytical representation (20), (24), and (27) shows that cell shapes correspond neither to a pure Saffman-Taylor form, nor to a pure parabolic form even at the tip, but to a finger with a rounded tip and straight sides. The details of the representation (20), (24), and (27) address neither the very vicinity of the tip which is at the dominant order circular, neither the far sides that are straight up to exponentially small deviations, but the intermediate region II in which a matching between these two asymptotic tendencies is achieved (Fig. 7). It is thus actually there that the differences between the fitting functions (8), (9), and (10) or between the different fits of function (8) are the largest. From this point of view, the present determination of cell shapes points to the compatibility between a rounded tip and a straight finger, the former being monitored by ρ and the latter by L. The resulting representation (20), (24), and (27) then indicates how the present advective-diffusive phase-change system sets the compromise. In this sense, the present work somewhat corresponds to an empirical version at intermediate Péclet number of the matching procedure undergone by Dombre and Hakim [6] at small Péclet number $Pe \ll 1$ or by Spencer and Huppert far from the cellular onset $V/V_c \gg k^{-1}$ [7].

B. Accuracy of the shape evolution

Although the representation (20) has been selected, other fitting functions (9) and (10) or other values of the retained exponent $n=1/2$ gave pretty close results that have only been rejected because of an overall slightly larger dispersion (Appendix, part 3) or values of fit parameter incompatible with a physical interpretation (Sec. IV A). In practice, these other determinations may be considered as also representative of the cell library. They thus enable us to measure the accuracy of our selection procedure.

In particular, the present determination (20) with ρ and L given by (14) and (15) can be used with confidence as far as the close determinations (8) with parameters (n,ρ,L) given in Figs. 9 and 10 or with n fixed to unity provide similar results. Then, both determinations actually give a relevant expression of cell form, even if the determination (14), (15), and (20) stands as the optimal one.

On the opposite, if a given issue reveals some noticeable difference depending on which of these determinations is chosen, then our procedure would have to be considered as not accurate enough in this instance. This, could arise on issues very sensitive to cell form, as for instance those involving noise amplification. Then, a finer analysis might have to be performed to determine the cell geometry to the level of accuracy required.

C. Relevance of fit parameters

By definition, the tip curvature radius $\hat{\rho}$ is given by differentiating the square of the representation function $f_{\tilde{\rho},\tilde{L}}(\cdot)$ at the tip:

$$\hat{\rho} = \left.\frac{\Lambda}{2}\frac{d^2 f_{\tilde{\rho},\tilde{L}}}{d\tilde{z}^2}\right|_0. \tag{29}$$

It is therefore a *local* variable, only dependent on the cell form *at* its tip. Similarly, the cell width $\hat{L}$ is given by the distance between cell grooves at the end of the observation window:

$$\hat{L} = 2\Lambda f_{\tilde{\rho},\tilde{L}}(\tilde{Z}). \tag{30}$$

It is therefore a *local* variable too, only dependent on the cell form *at* the window boundary.

The link between these geometrical variables and fit parameters follows from the properties (4) and (5) of $f_{\tilde{\rho},\tilde{L}}(\cdot)$:

$$\hat{\rho} = \frac{\Lambda}{2}2\tilde{\rho} = \rho, \tag{31}$$

$$\tilde{Z} \gg \tilde{\rho}: \hat{L} \approx 2\Lambda\frac{\tilde{L}}{2} = L. \tag{32}$$

Compared to the local nature of $\hat{\rho}$ and $\hat{L}$, the values of the fit parameters $(\tilde{\rho},\tilde{L})$ are adjusted so that the fitting function matches the cell form *all along* the cell. They are thus determined in a *nonlocal* way which contrasts with the *local* character of the tip curvature radius and of the cell spacing to which they *a priori* reduce in the corresponding regions. In particular, the values of the nonlocal fit parameters (ρ,L) obtained here differ from those of the analogous fit parameters determined in reduced tip or grooves domains [22]. This results from the fact that fit parameters different from the optimal values for specific regions are nevertheless more suited in intermediate regions and, finally to the whole shape. In addition, nonlocal fit parameters obtained from different fit functions (8), (9), and (10) also differ one from the other, although they yield representations that match a given form equally well. This comes from the fact that different fit functions correspond to different statistical weights along the shape and thus to different kinds of determinations of optimal parameters.

According to these statements, the shape determination (20) should be considered as a *whole*. In particular, considering fit parameters solely should only be done with caution since their meaning *a priori* makes sense only within the whole shape representation. With this in mind, we analyze below the curvature radius ρ.

D. Tip curvature radius

In order to determine the sensitivity of the value of the curvature radius $\hat{\rho}=\rho$ to the fitting function, we compare below the values obtained for four different kinds of fits performed on the whole library.

The form (6) with the generating function (9) and free parameters $(n,\tilde{\rho},\tilde{L})$. This gives parameters (33).

The form (6) with the generating function (8) and free parameters $(n,\tilde{\rho},\tilde{L})$. This gives parameters (34).

The form (6) with the generating function (8), free parameters $(\tilde{\rho},\tilde{L})$ and fixed parameters $n=1/2$ or $n=1$. This gives Table I for $n=1/2$ and parameters (35) for $n=1$.

Although noticeable variations could be feared, one obtains close parameters for the power law (11) that describes $\rho(V,\Lambda,G)$:

$$e_V = -0.28, \quad e_\Lambda = 0.73, \quad e_G = 0.44, \tag{33}$$

$$e_V = -0.28, \quad e_\Lambda = 0.71, \quad e_G = 0.47, \tag{34}$$

$$e_V = -0.26, \quad e_\Lambda = 0.79, \quad e_G = 0.49. \tag{35}$$

The weakness of these variations means that the fit parameter ρ is robust with respect to the present fitting procedures. This is coherent with the fact that it showed no coupling with the spurious variations of the other parameters L,n (Fig. 10). This gives confidence for comparing it to the tip curvature radius determined in a more local way, i.e., from parabolic fits performed around the cell tips [22].

Parabolic fits actually depends on the size of the fitting window applied around cell tips [4,22]. This, *a priori*, makes their determination dependent on an extrinsic parameter, and thus somewhat arbitrary. However, it appears that in a given range of window sizes, the determination of curvature radius is stable. Considering the corresponding values as the relevant ones, we obtained the following rounded values for the power law exponents: $(e_V,e_\Lambda,e_G)=(-1/3,3/4,1/2)$ [22].

These rounded exponents are the same as those found by the present global fit except for the exponent e_V which is slightly smaller. This indicates that, once one has found the narrow tip region in which parabolic fits performed in different windows provide the same result, the resulting curvature agrees with that which could result from a global fit of the whole shape. However, the difference between the two procedures is that one has to pay a large attention to the fitting window in the former whereas the latter is independent of such consideration.

The rounded exponents (14) and (15) yield:

$$\rho = 0.095V^{-1/4}\Lambda^{3/4}G^{1/2}, \tag{36}$$

$$\frac{\rho}{L} \approx 0.144V^{-1/3}\Lambda^{-1/4}G^{1/2}, \tag{37}$$

$$L = 0.66V^{-1/10}\Lambda. \tag{38}$$

This confirms that increasing thermal gradient at otherwise unchanged parameters (V,Λ) makes tip fatter, as expected from the tightening of the isothermal lines. However, the effect is less than proportional to the thermal gradient, i.e., less than the tightening of the thermal field. On the other hand, the negative value of the exponent of the velocity for ρ corroborates the fact that the quicker the cell, the thinner it is. This remains true relatively to the cell width L, since the sharpness $\rho/L \approx V^{-1/3}$ of the cell also decreases with velocity. This form evolution is however less pronounced than in free growth where $\rho \approx V^{-1/2}$ instead [1,18].

Relation (36) also shows that ρ varies with the cell spacing Λ, but less than proportionally: $\tilde{\rho}=\rho/\Lambda \propto \Lambda^{-1/4}$. Accordingly, there is no pure geometrical similarity even at the same thermal gradient G or at the same pulling velocity V. On the other hand, the cell width L follows the cell spacing: $\tilde{L}=L/\Lambda \propto \Lambda^0$. This is at variance with Saffman-Taylor forms (2) in which the reduced curvature radius $\tilde{\rho}=\rho/\Lambda$ and the reduced cell width $\tilde{L}=L/\Lambda=\lambda$ are linked one to the other according to $\pi\tilde{\rho}(1-\tilde{L})=\tilde{L}^2$. For similar reasons, this is also incompatible with a Saffman-Taylor shape matching a Scheil profile [6]:

$$\pi\tilde{x} = [1+(\lambda-1)(1+\alpha_0\tilde{z})^{-\beta}]\arccos\left[\exp\left(-\frac{\pi\tilde{z}}{1-\lambda}\right)\right], \tag{39}$$

where α_0 and β stand as fixed parameters. In particular, at a fixed bound $Z \gg \rho$ of the observation window [Fig. 7(b)], the observed reduced cell width $\tilde{L}$ would still be linearly related to the parameter λ:

$$\tilde{L} = 1 + (\lambda - 1)(1 + \alpha_0 Z)^{-\beta} \quad (40)$$

so that the same conclusion as for a pure Saffman-Taylor form would be reached. More generally, the absence of similarity between ρ and L denies the existence of a one parameter family for representing cell shapes in the present parameter range.

E. Regularity of the shape evolution

In the above fitting procedure, no significant difference between steady or weakly dendritic cells and moderately dendritic cells could be noticed with regard to the dependence of fitting parameters with control parameters (see Table I). In particular, all forms were accurately fitted with the same function (20) with parameters varying according to the same power law (11) and (12) and the same prefactors and exponents (14) and (15). This means that, regarding the cell shape, steady and moderately dendritic cells belong to the same branch of solution. In particular, *no step* in the parameters n, L, ρ, nor in their evolution with the control parameters (e.g., in the exponents of their variation) could be detected. The former (latter) continuity attests of the absence of first-order (second-order) transition at the occurrence of sidebranching.

This regularity of the shape evolution between steady cells and moderately dendritic cells means that, to the present accuracy, there exists no shape transition at the cell-dendrite transition, i.e., no change of branch of solution. This corroborates the evidence of sidebranching as a dynamical phenomenon superimposed to the cell shape on either of the crystal directions [9].

The absence of transition for cell shape must not be confused with the sudden variation of the mean cell spacing $\bar{\Lambda}$ that has been reported at the cell to dendrite transition [16]. In particular, the latter addresses not cell shapes but cell spacings seen in average. In addition, whereas the present shape evolution refers to the *steady* states of cells displaying a *definite* spacing, the observation of mean cell spacing variation relies on an *average* over the different cells of an interface and over different runs, i.e., over *different* cell spacings and *different* dynamical conditions. Accordingly, it refers to the length of the available range for cell spacing and to the cell spacing distribution in it. Our study then shows that, even if the range of available cell spacings suddenly varies, the cell form for each of them taken separately does not. Accordingly, the branch of solution for directional growth remains the same, even if the spacing range and/or the distribution of spacings vary.

Although this result clarifies an important solidification feature at the cell to dendrite transition, it *a priori* leaves undetermined the nature of the sudden variation of cell spacing evidenced there [16]. However, experimental determination of the cellular instabilities as a function of cell spacing and of pushing velocity reveals a striking coincidence: a drastic elimination of a large range of small cells occurs at velocities for which large cells begin to emit sidebranches [13,23]. Accordingly, two uncorrelated events occur along the cellular interface at the same pushing velocity: one yields evidence of sidebranch emission, i.e., of dendrites; the other implies a sudden increase of the mean cell spacing by elimination of a large range of small cells. Taken together, they might give the impression of a link between them whereas they actually refer to instabilities of different nature.

F. Perspective

The cell shape representation obtained here synthetically handles the form evolution of cells in the control parameter space. This should potentially offer relevant interactions with simulation and theory.

At first, this determination opens the path for a detailed comparison with numerical simulations of directional solidification cells, in either two or three dimensions, one-sided or two-sided models, and length scales d_0 and l_T close or weakly distant from those of our experiment. This could be a way of evaluating the importance of the simplifications made to the minimal model of solidification or to its parameters. On the other hand, the accurate experimental forms that follow from our determination should be tested against instability so as to obtain agreement with experimental [13] or theoretical instability diagrams. This, in particular, should worth being done for the sidebranching instability which could be quite form-sensitive according to noise-amplification mechanisms [24].

On the other hand, although the analytical fit function (8) simply corresponds to a partially arbitrary choice, the resulting determination (20), (11), and (12) provides the actual steady cell shapes from tip to grooves in a large region of the control parameter space. This shape and its evolution are thus representative of the equilibrium between advection, diffusion and impurity rejection within the minimal model of directional solidification. Recovering this shape evolution from a theoretical side would thus provide us with a valuable improvement of our understanding of the balances that drive the shapes of these growth interfaces. In this spirit, a comparison of our experimental determination of cell shape with the predictions of the theories of Dombre and Hakim [6] or Spencer and Huppert [7] extended to our regime would be especially interesting. The former comparison could state whether, as indicated in Sec. VI D, a matching between a Scheil profile and a Saffman-Taylor profile fails in capturing cell shapes in directional solidification. As the determination of Spencer and Huppert relies on no surface tension [7], the latter comparison would be expecially interesting to conclude about the importance of surface tension effects regarding cell shape in directional solidification.

VII. CONCLUSION

The shape of steady cells stands as one of the most important features in directional solidification. In particular, cell shape partly determines the flux between the various thermodynamic phases and, thus, the conditions required to maintain steady growth states or to trigger the occurrence of instabilities on cells or on cell arrays. At the intermediate Péclet regime that is relevant to experiments, cell shapes largely differ from those proposed at asymptotic Péclet num-

ber regimes on a theoretical basis. In the absence of a relevant theory, a direct determination of cell geometry, whatever it is, then stands as a relevant goal. We have achieved it in directional solidification of a succinonitrile alloy.

For this, a fitting procedure has been applied on each cell among a large experimental library. Different fit functions were used with enough few parameters to avoid spurious fluctuations of them from cell to cell. In addition, fitting of forms has been achieved on the whole observed profile, starting from cell tip and ending at cell grooves. The average evolution of the fitting parameters with the control parameters of the system have then been considered, yielding a final representation of cell forms which has been validated on the whole cell library.

By this procedure, cell forms and their evolution have been determined in large domains of both the real space and the control parameter space. The resulting generating function (20), (24), and (27) then simply gathers the evolution of cell shape in this system. Beyond this, it calls for theoretical and numerical investigations capable of understanding its structure. This in particular offers a stimulating opportunity for better modeling the equilibrium between advection, diffusion, rejection and surface tension on free boundaries and for validating instability mechanisms such as that which prevails in sidebranching. Finally, similar procedures applied on other kinds of growth systems would enable one to compare the form of their interfaces on the same rational basis, so as to determine whether directional solidification and other interface growth systems share similar properties or refer to specific dynamics.

ACKNOWLEDGMENTS

We thank S. Bodea for stimulating discussions.

APPENDIX

We analyze the results of the independent fits of cell shapes so as to evidence coherent evolutions of the fitting parameters $(\tilde{\rho},\tilde{L},n)$ with the control parameters (V,Λ,G). The coupling between fitting parameters, that is inherent to the fitting procedure, will yield us to fix one of them so as to make the selection of the optimal parameter sharper.

1. Fitting parameters $(\tilde{\rho},\tilde{L},n)$

Fitting relation (8) on the steady or moderately dendritic cells of the library yields in Figs. 9 and 10 the following behavior.

(i) Exponents n fluctuate in between 0.4 and 0.8 with no definite tendency. In particular, its variation with V at fixed n and G (Fig. 9) shows nonmonotonous evolutions whose forms differ depending on G and Λ: a "hat" form at $G=140$ K cm^{-1}, $\Lambda=90$ μm and a decrease followed by a plateau at $G=78$ K cm^{-1}, $\Lambda=130$ μm. This sensitivity to G seems more an artifact than an actual change of behavior of the growth phenomenon. This is confirmed by the variation of n with Λ at fixed V and G (Fig. 10) which shows large sudden variations that are correlated with those exhibited by L, especially in Fig. 10(b). Notice finally that, in average over the cell library, exponent n takes a mean value close to 0.5.

(ii) The fit parameter L shows coherent evolutions with V and Λ. At fixed Λ and G, L appears somewhat constant with respect to V (Fig. 9). At fixed V and G, L shows a monotonous growth with Λ including fluctuations that are correlated to those shown by exponent n, especially in Fig. 10(b).

(iii) The fit parameter ρ shows coherent evolutions with V and Λ. At fixed Λ and G, ρ regularly decreases with V (Fig. 9). At fixed V and G, ρ regularly increases with Λ (Fig. 10).

This analysis shows that ρ varies smoothly among the shape library. This contrasts with L and n which involve sharp variations, especially n which displays the largest incoherent variations. These sudden changes of n with V at fixed Λ and G might point to characteristic velocities in the observed data range. Instead, we shall consider them as irrealistic variations brought about by the coupling with the two other fit parameters: L and ρ. This interpretation is supported by the evidence of correlations between the fluctuations of n and L with Λ at fixed V and G (Fig. 10).

On the other hand, the fact that L is quasiconstant with respect to V at fixed Λ and G is also puzzling since one would have expected a monotonous variation. This, together with the correlation of the variations of L and n with Λ, leads us to also suspect the variable L to partly result from a coupling with exponent n.

Following these statements, we address below the implications of separately fixing the two parameters L and n and look for determining which is the most meaningful. The value of L will be fixed to the definite value Λ: $\tilde{L}=1$. The value of n will be fixed to the simplest value consistent with its average: $n=0.5$ for free $\tilde{L}$ and, as found below, $n=1$ for $\tilde{L}=1$.

2. Fitting parameters $(\tilde{\rho},n)$ with $\tilde{L}=1$

Fixing $\tilde{L}=1$, i.e., $L=\Lambda$, we obtain fits of cell shapes that are less satisfactory than previously, especially in region II. Beyond the fact that reducing fit parameters can only weaken the quality of optimization, this indicates that other values than $\tilde{L}=1$ would well be worth being addressed, so that $\tilde{L}$ should be let free.

Although the fits at $\tilde{L}=1$ will not be further analyzed, they nevertheless provide useful indications of the relevant values to consider for fixing n. These values have been found to fluctuate from cell to cell, but around a mean close to unity that is about twice the value found from the three-parameters fit of Appendix, part 1. This indicates a relevant common value for n that is twice than before: $n=1$.

3. Fitting parameters $(\tilde{\rho},\tilde{L})$ with $n=0.5$ or $n=1$

Following the result of the above fits, there appears two relevant common values for n on the whole library: $n=0.5$ (Appendix, part 1) or $n=1$ (Appendix, part 2). Imposing them, we obtain fits that approximate each cell form at nearly

the same level of accuracy as when the exponent n was allowed to freely vary. In particular, the discrepancy between the actual forms and the fitted forms is always below three pixels whatever the region of the shape is considered [Figs. 12(a) and 12(b)], provided of course that no sidebranch is emitted [Fig. 12(c)].

[1] A. Papapetrou, Z. Kristallogr. **92**, 89 (1935); G. P. Ivantsov, Dokl. Akad. Nauk SSSR **58**, 56 (1947).
[2] P. Pelcé and A. Pumir, J. Cryst. Growth **73**, 337 (1985).
[3] E. A. Brener, M. B. Geilikman, and D. E. Temkin, Zh. Eksp. Teor. Fiz. **94**, 241 (1988) [Sov. Phys. JETP **67**, 1002 (1988)].
[4] P. Kurowski, C. Guthmann, and S. de Cheveigné, Phys. Rev. A **42**, 7368 (1990).
[5] A. Pocheau and M. Georgelin, J. Cryst. Growth **206**, 215 (1999).
[6] T. Dombre and V. Hakim, Phys. Rev. A **36**, 2811 (1987).
[7] B. J. Spencer and H. E. Huppert, Acta Mater. **45**, 1535 (1997); B. J. Spencer and H. E. Huppert, J. Cryst. Growth **200**, 287 (1999).
[8] J. D. Hunt, K. A. Jackson, and H. Brown, Rev. Sci. Instrum. **37**, 805 (1966).
[9] M. Georgelin and A. Pocheau, Phys. Rev. E **57**, 3189 (1998).
[10] The existence of thermal boundary layer prevents the thermal gradient at the front G to be inversely proportional to the gap g.
[11] C. Huang and M. E. Glicksman, Acta Metall. **29**, 701 (1981).
[12] L. M. Williams, M. Muschol, X. Qian, W. Losert, and H. Z. Cummins, Phys. Rev. E **48**, 489 (1993).
[13] M. Georgelin and A. Pocheau, in *Dynamics and Morphogenesis of Branching Structures from Cells to River Networks*, edited by V. Fleury, J-F. Gouyet, and M. Leonetti (EDP Sciences, Springer, New York, 1999), pp. 409–415.
[14] J. T. C. Lee and R. A. Brown, Phys. Rev. B **47**, 4937 (1993).
[15] M. Georgelin and A. Pocheau, Phys. Rev. Lett. **79**, 2698 (1997).
[16] B. Billia and R. Trivedi, *Handbook of Crystal Growth* (Elsevier Science, New York, 1993), Vol. 1, Chap. 14.
[17] P. G. Saffman and G. I. Taylor, Proc. R. Soc. London, Ser. A **245**, 312 (1958).
[18] M. Ben Amar and E. Brener, Phys. Rev. Lett. **71**, 589 (1993); E. Brener, Phys. Rev. Lett. **71**, 3653 (1993).
[19] E. Brener and D. Temkin, Phys. Rev. E **51**, 351 (1995).
[20] U. Bisang and J. H. Bilgram, Phys. Rev. E **54**, 5309 (1996).
[21] T. F. Bower, H. D. Brody, and M. C. Flemmings, Trans. Metall. Soc. AIME **236**, 624 (1966); H. D. Brody and M. C. Flemmings, Trans. Metall. Soc. AIME **236**, 615 (1966).
[22] M. Georgelin and A. Pocheau, J. Cryst. Growth **268**, 272 (2004).
[23] A. Pocheau and M. Georgelin, J. Phys. IV **11**, 169 (2001).
[24] P. Pelcé, and P. Clavin, Europhys. Lett. **3**, 907 (1987); J. S. Langer, Phys. Rev. A **36**, 3350 (1987); S. K. Sarkar, Phys. Lett. A **117**, 137 (1986).